Article

Superconducting-qubit readout via low-backaction electro-optic transduction

https://doi.org/10.1038/s41586-022-04720-2

Received: 20 September 2021

Accepted: 4 April 2022

Published online: 15 June 2022

Check for updates

R. D. Delaney[1,2]✉, M. D. Urmey[1,2], S. Mittal[1,2], B. M. Brubaker[1,2], J. M. Kindem[1,2], P. S. Burns[1,2], C. A. Regal[1,2] & K. W. Lehnert[1,2,3]

Entangling microwave-frequency superconducting quantum processors through optical light at ambient temperature would enable means of secure communication and distributed quantum information processing[1]. However, transducing quantum signals between these disparate regimes of the electro-magnetic spectrum remains an outstanding goal[2–9], and interfacing superconducting qubits, which are constrained to operate at millikelvin temperatures, with electro-optic transducers presents considerable challenges owing to the deleterious effects of optical photons on superconductors[9,10]. Moreover, many remote entanglement protocols[11–14] require multiple qubit gates both preceding and following the upconversion of the quantum state, and thus an ideal transducer should impart minimal backaction[15] on the qubit. Here we demonstrate readout of a superconducting transmon qubit through a low-backaction electro-optomechanical transducer. The modular nature of the transducer and circuit quantum electrodynamics system used in this work enable complete isolation of the qubit from optical photons, and the backaction on the qubit from the transducer is less than that imparted by thermal radiation from the environment. Moderate improvements in the transducer bandwidth and the added noise will enable us to leverage the full suite of tools available in circuit quantum electrodynamics to demonstrate transduction of non-classical signals from a superconducting qubit to the optical domain.

Superconducting quantum computers using arrays of transmon qubits are a leading platform for scalable quantum computation[1]. However, these devices must operate at temperatures below 100 mK, with quantum information encoded in microwave fields that would be corrupted by thermal noise if transmitted at ambient temperature. In contrast, optical quantum networks are a well established technology for the transmission of quantum states over long distances, and do not require low temperatures[16–18]. Thus, a quantum-enabled electro-optic transducer linking the microwave and optical domains would greatly expand the capabilities of quantum information science.

The pursuit of an optical quantum network of superconducting qubits has given rise to a rich research field searching for efficient, low-noise electro-optic transduction techniques[2–9]. Although electro-optic elements have been demonstrated as useful tools for delivering classical signals to superconducting circuits[19,20], devices designed to transduce quantum states must satisfy a different and more stringent set of requirements[21]. In spite of substantial recent progress, it remains an outstanding challenge to combine these transducers with superconducting qubits in a manner that does not interfere with the operation of the qubit. An impressive recent experiment demonstrated the transduction of photons from a superconducting qubit to the optical domain[9], but an attempt to use this device to create entanglement between the qubit and optical pulse would be disrupted by the optical pump required for transduction. Furthermore, such piezo-optomechanical transducers require a specific piezoelectric materials platform for qubit fabrication, complicating the introduction of some recent advances in modular circuit quantum electrodynamics (cQED)[22–24].

In this work, we demonstrate readout of a superconducting transmon qubit embedded in a three-dimensional (3D) cQED architechture through a low-backaction electro-optomechanical transducer. The transducer imparts minimal backaction on the qubit, equivalent to only $\Delta n = (3 \pm 1) \times 10^{-3}$ photons in the microwave readout cavity dispersively coupled to the qubit. Although the transduction bandwidth is relatively narrow, the operation of the transducer is continuous rather than pulsed[7–9], enabling efficiency and repetition rates far exceeding the values demonstrated by a device that integrates the transducer and the qubit on the same chip[9]. We then use the superconducting qubit as a non-Gaussian resource to characterize the quantum efficiency[25] with which we transduce signals from the cQED system to the optical domain.

The experiment consists of two modular systems attached to the base plate of an optical-access dilution refrigerator at a base-plate temperature $T_{bp} \approx 40$ mK. The first of these (Fig. 1a) is a cQED system comprising a transmon qubit dispersively coupled to a quarter-wave coaxial cavity resonator[22]. The microwave cavity has a total linewidth of $\kappa_c/2\pi = 380$ kHz, whereas the dispersive interaction between the qubit and the cavity causes a state-dependent shift of the cavity's resonant

[1]JILA, National Institute of Standards and Technology and the University of Colorado, Boulder, CO, USA. [2]Department of Physics, University of Colorado, Boulder, CO, USA. [3]National Institute of Standards and Technology, Boulder, CO, USA. ✉e-mail: robert.delaney@colorado.edu

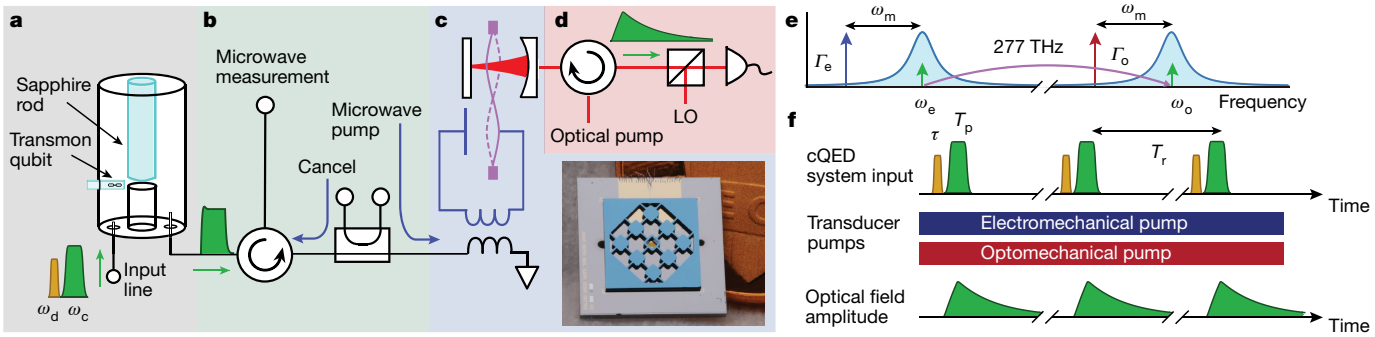

Fig. 1 | Apparatus for readout of a superconducting qubit via electro-optic transduction. a, A cQED system consisting of a transmon qubit dispersively coupled to a 3D coaxial quarter-wave cavity resonator. A translatable sapphire rod tunes the frequency of the cavity in situ. Qubit preparation pulses with frequency ω_d (gold), followed by readout pulses with frequency ω_c (green), are injected through the cQED system's input line. **b**, A directional coupler is used to apply the microwave pump to the transducer, while the circulators enable microwave heterodyne measurement of reflected signals. Isolation between the cQED system and the transducer is achieved using circulators, along with the directional coupler for interferometric cancellation. **c**, The electro-optic transducer consists of an optical cavity and a flip-chip microwave inductor-capacitor (LC) circuit resonator simultaneously coupled to a single mode of a high-quality-factor silicon-nitride membrane with frequency $\omega_m/2\pi = 1.45$ MHz. Inset: image of flip chip containing the silicon-nitride membrane, phononic shielding and the LC circuit, with a penny in the background for scale. **d**, Optical pump and heterodyne detection scheme. **e**, Transducer pumps and experimental readout signals represented in the frequency domain. The electro(opto)-mechanical damping rates Γ_e (Γ_o) are controlled by the strength of the respective pumps, both red-detuned by ω_m to transduce microwave signals to the optical domain. **f**, A pulse timing diagram illustrates the qubit (gold) and readout (green) pulses, with the experiment conducted with a repetition time of $T_r = 0.4$–2 ms and steady-state pumps. The upconverted readout pulse is filtered by the transducer's frequency response (bottom).

frequency by $2\chi/2\pi = 344$ kHz; thus $\kappa_c/2\chi \approx 1$, the optimal value for low-power dispersive readout of the qubit[26]. The microwave cavity's resonant frequency ω_c can be tuned in situ by a sapphire rod (Fig. 1a) attached to a piezoelectric stepping module, enabling the microwave resonance of the cQED system to be brought into resonance with the transducer's microwave mode at $\omega_e/2\pi = 7.938$ GHz (Methods).

The other experimental module (Fig. 1c) is an electro-optic transducer containing microwave and optical resonators coupled to a single mode of a silicon-nitride membrane with a mechanical resonance frequency of $\omega_m/2\pi = 1.45$ MHz (refs. [4,27]). Simultaneously applying strong microwave and optical pumps red-detuned by ω_m (Fig. 1e) enhances the parametric coupling to the mechanical resonator[4]. This enables microwave (optical) photons to be swapped through a beamsplitter interaction with phonons at a rate Γ_e (Γ_o) far exceeding the intrinsic mechanical dissipation rate of $\gamma_m = 2\pi \times 0.11$ Hz. The low mechanical dissipation is enabled by phononic shielding that yields a bandgap centred on ω_m (Methods). An incident signal on resonance with the microwave (optical) resonator will then be transduced to the optical (microwave) domain with the bandwidth of the process determined by the total damping rate $\Gamma_T = \Gamma_e + \Gamma_o + \gamma_m$.

Our qubit readout scheme starts with the dispersive interaction between the qubit and the microwave cavity, which causes the cavity's resonant frequency $\omega_c \pm \chi$ to depend on whether the qubit is prepared in the ground state or the excited state[28]. Thus, if a short readout pulse centred at ω_c is applied to the microwave cavity input line (Fig. 1a), the phase of the emitted microwave pulse will depend on the state of the qubit. This microwave pulse is then routed to the electro-optic transducer through elements used to isolate the qubit from transducer backaction (Fig. 1b, Methods), and the upconverted readout pulse at wavelength $\lambda = 1{,}084$ nm is demodulated using balanced heterodyne detection (Fig. 1d). During qubit readout experiments, the transducer pumps are applied continuously, whereas qubit preparation and readout pulses are repeated at intervals T_r ranging from 0.4 ms to 2 ms depending on the bandwidth of the transducer. The bandwidth of the transducer filters the upconverted readout pulse as shown in the bottom row of Fig. 1f, which sets the upper limit on T_r.

To initialize the qubit state, a short qubit drive pulse with frequency ω_d and duration τ (gold pulse in Fig. 2a) can be applied to the input line of the cQED system to induce Rabi oscillations in the qubit at a rate Ω_r. For $\tau = \pi/\Omega_r$, the qubit population is inverted, and prepared mainly in the excited state $|e\rangle$. When no pulse is applied ($\tau = 0$), the qubit is prepared mainly in the ground state $|g\rangle$. State preparation is followed by a square readout pulse of length $T_p = 15$ μs (green pulse in Fig. 2a). The maximum useful length of the readout pulse, and hence the minimum bandwidth, is determined by the lifetime of the qubit ($T_1 = 17$ μs)[29]. The pulse then travels through the cavity and is upconverted as described above, and the demodulated optical signal is digitized, appropriately weighted[29] (Supplementary Information) and integrated to extract a single voltage encoding the state of the qubit.

We first use this protocol to demonstrate single-shot readout of the superconducting qubit through the electro-optic transducer. By recording multiple voltage traces to form histograms of the qubit state-dependent optical heterodyne voltage, we can estimate the single-shot probability $P(e)$, and choose a voltage threshold V_{thresh} (dashed line in Fig. 2b) to maximize the fidelity $F_{opt} = 1 - P(e|g) - P(g|e)$, where $P(e|g)$ ($P(g|e)$) is the probability of measuring $|e\rangle$ ($|g\rangle$) given that $|g\rangle$ ($|e\rangle$) was prepared. In Fig. 2b, we show histograms of the optical heterodyne voltage when preparing the qubit in either $|e\rangle$ or $|g\rangle$. The amplitude of the microwave readout pulse incident on the cQED system's microwave cavity is $\sqrt{\bar{n}_r} \approx 19$ photons$^{1/2}$, and the electro-optic transducer is operated continuously with $(\Gamma_e, \Gamma_o)/2\pi = (0.5, 2.4)$ kHz to transduce the emitted microwave field to the optical domain for detection. A bimodal distribution is clearly visible in each histogram, with the two modes corresponding to the ground and excited states of the qubit. We find a maximum readout fidelity of $F \approx 0.4$, limited by inefficient measurement and the residual excited-state population in the qubit (Supplementary Information).

We can then use the electro-optic transducer to measure Rabi oscillations of the superconducting qubit and demonstrate the stability of the optical measurement apparatus. To measure Rabi oscillations, we vary the qubit drive pulse length τ and the pulse frequency ω_d (Fig. 2c, with the same pulse amplitude and transducer damping rates as in Fig. 2b). This measurement was taken over approximately 1.5 h using a single threshold value chosen at the beginning of the experiment, indicating the stability of the electro-optic transducer over this period of time.

Next, we characterize backaction from the transducer on the qubit. It is critical to minimize this excess backaction as it can limit the fidelity of qubit entanglement and post-selection operations[15] (Methods).

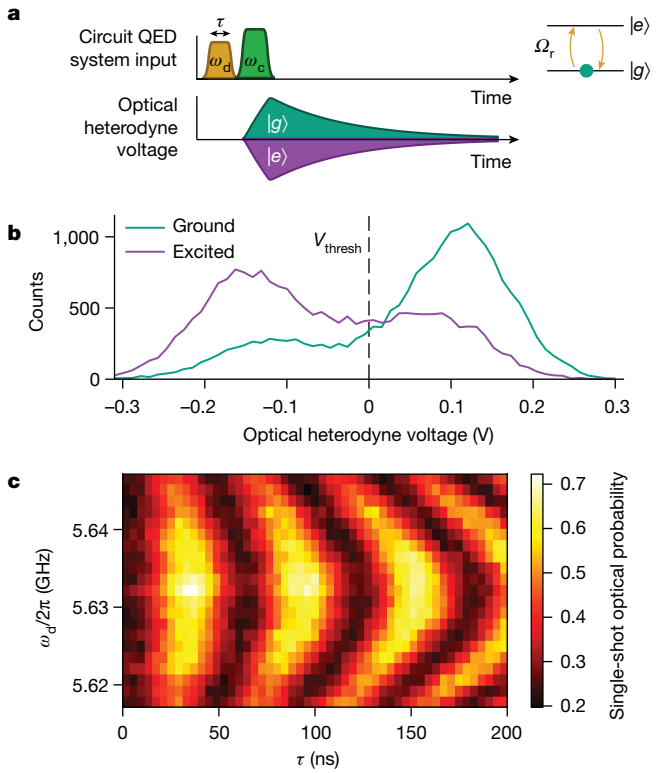

Fig. 2 | Single-shot readout of a transmon qubit via the electro-optic transducer. a, A microwave drive pulse with frequency ω_d near the qubit frequency and length τ is applied to drive Rabi oscillations in the qubit at rate Ω_r. A microwave readout pulse centred around ω_c is sent through the cavity and subsequently transduced to the optical domain for optical heterodyne detection. The phase of the optical pulse depends on the state of the qubit. Pulse widths are not to scale for clarity. **b**, Histogram of optical heterodyne voltage when reading out the superconducting qubit through the electro-optic transducer. A 15-μs microwave pulse ($\sqrt{\bar{n}_r} \approx 19$ photons$^{1/2}$) is applied to the microwave cavity to read out the state of the superconducting qubit when preparing it in the ground state (teal curve) or excited state (purple curve), with $(\Gamma_e, \Gamma_o)/2\pi = (0.5, 2.4)$ kHz. The dashed line represents the voltage threshold V_{thresh} for single-shot readout. **c**, Rabi oscillations measured through the transducer with the same readout pulse and transducer parameters as above.

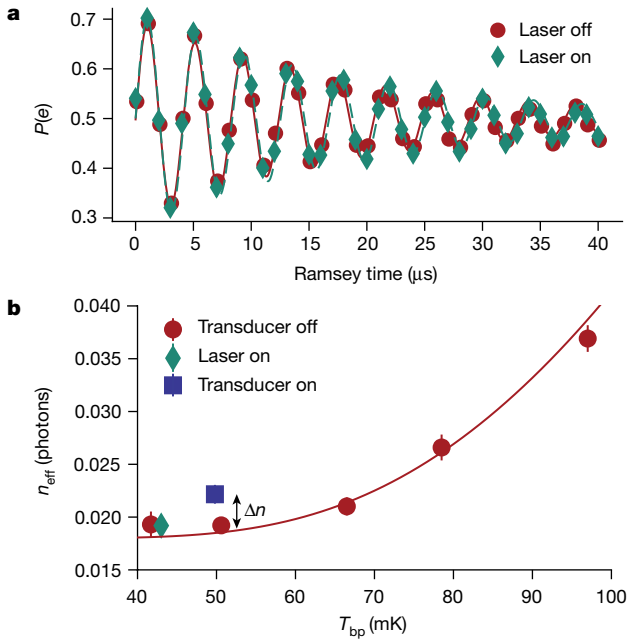

Fig. 3 | Transducer backaction on the qubit. a, Microwave-domain Ramsey experiment with the transducer off ($(\Gamma_e, \Gamma_o) = (0, 0)$; red circles) and with the laser on ($(\Gamma_e, \Gamma_o)/2\pi = (0, 5.0)$ kHz; cyan diamonds). The lines are fits to the data. **b**, Effective thermal occupancy of the cQED system's microwave cavity as a function of the dilution refrigerator base-plate temperature T_{bp}. Red circles are data obtained with the transducer off, and the line is theory. The cyan diamond indicates the occupancy of the microwave cavity with $\Gamma_o/2\pi = 5.0$ kHz, indicating no additional dephasing of the qubit from the laser. The blue square is the effective occupancy while operating the transducer at $(\Gamma_e, \Gamma_o)/2\pi = (1.1, 5.0)$ kHz. There is a small amount of excess backaction equivalent to $\Delta n = (3 \pm 1) \times 10^{-3}$ photons in the microwave cavity. Error bars represent one standard deviation.

An ideal electro-optic transducer performs unitary operations on the microwave and optical fields, and need not add noise or impart backaction during the transduction process[30]. However, under real experimental conditions, the effective thermal bath n_{eff} coupled to the cQED system imparts backaction on the qubit in the form of shot noise from microwave photons randomly arriving in the cavity. For $n_{eff} \ll 1$, these photons cause dephasing of the qubit at a rate Γ_ϕ[31]

$$\Gamma_\phi = \frac{\kappa_c \chi^2}{\frac{\kappa_c^2}{4} + \chi^2} n_{eff}, \quad (1)$$

where we can split the effective occupancy $n_{eff} = n_{th} + \Delta n$ into a thermal component n_{th} and a component describing excess backaction Δn from the transducer. Such backaction can arise due to heating of the cQED device, through bulk heating or from thermal radiation emitted by the electro-optic transducer, and more than 110 dB of microwave pump suppression is required to make coherent pump backaction negligible. This is achieved using a combination of circulators and interferometric cancellation[32] of the strong microwave pump required for efficient transduction (Fig. 1b, Methods).

We first measure the effect of the optical pump on the cQED system, with the microwave pump off. In Fig. 3a, a microwave-domain Ramsey experiment is performed to measure the coherence time T_2 of the qubit when the laser is off (red circles) and when it is on with $\Gamma_o/2\pi = 5.0$ kHz (cyan diamonds), achieved with 11 mW of circulating power in the optical cavity. Heating of the cQED system by the laser would dephase the qubit and reduce its coherence time. We find $T_{2,on} = 20.7 \pm 0.2$ μs and $T_{2,off} = 20.4 \pm 0.2$ μs, showing no measurable change in the qubit coherence time owing to laser illumination.

We can expand the scope of this measurement, and additionally measure the lifetime of the qubit to determine its dephasing rate $\Gamma_\phi = T_\phi^{-1} = T_2^{-1} - \frac{1}{2}T_1^{-1}$, and infer the effective occupancy n_{eff} of the cQED system's microwave cavity using equation (1). In Fig. 3b, we plot this effective occupancy as the temperature of the dilution refrigerator's base plate T_{bp} is varied. At low temperature, the inferred thermal occupancy plateaus at $n_{th} \approx 0.019$ photons ($T_{eff} = 95$ mK), although this plateau may be caused by intrinsic sources of qubit dephasing other than an elevated temperature[33]. The cyan diamond in Fig. 3b demonstrates that there is no measurable excess backaction from the laser ($\Gamma_o/2\pi = 5.0$ kHz) on the qubit. We then turn on the microwave pump ($\Gamma_e/2\pi = 1.1$ kHz, leaving Γ_o unchanged) and the blue square in Fig. 3b indicates excess backaction of $\Delta n = (3 \pm 1) \times 10^{-3}$ photons. The error bars represent the statistical error resulting from repeated measurements of the T_1 and T_2 time of the qubit to infer Δn (Methods). This excess backaction comes largely from local heating of microwave components by the strong microwave pump with incident power $P_{inc} = -45$ dBm (Methods). These backaction measurements are taken at the largest values of Γ_o and Γ_e used in this work, and backaction is expected to be even lower when operating at smaller Γ_e.

The final figure of merit for electro-optic qubit readout is the quantum efficiency η_q, which is a measure of how well the optical measurement

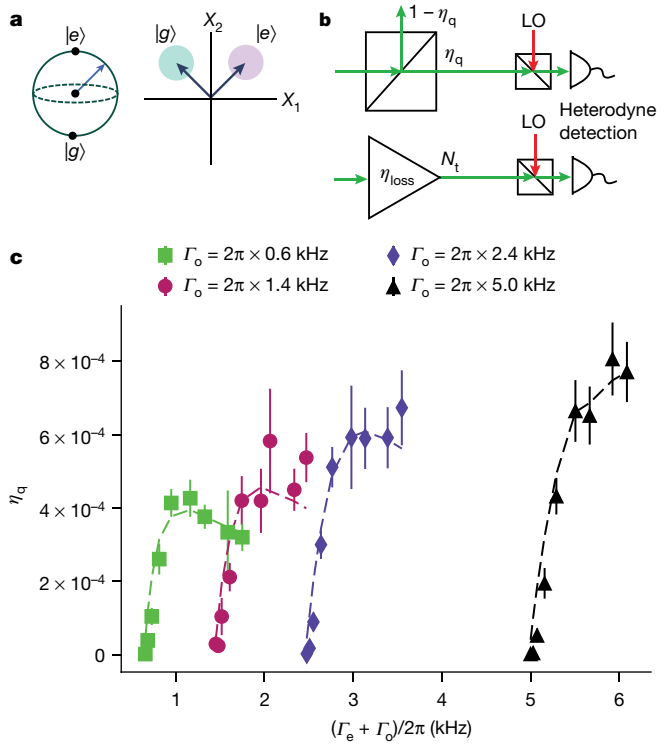

Fig. 4 | Quantum efficiency of electro-optic readout of a superconducting qubit. a, During dispersive readout, the state of the qubit is mapped onto one of two (microwave) coherent states, which is then upconverted and detected in heterodyne. The quantum efficiency η_q is a measure of how well the optical measurement apparatus can distinguish these two coherent states. **b**, The optical measurement apparatus can be modelled as a beamsplitter with effective transmissivity η_q followed by an ideal heterodyne detector. Alternatively, it can be modelled as an amplifier with gain $\eta_{loss} = \eta_q/\eta_{noise}$ and output-referred added noise N_t, whose output is directed towards an ideal heterodyne detector. **c**, The quantum efficiency is calibrated by comparing the signal-to-noise ratio of the electro-optic qubit readout measurement to the total measurement-induced dephasing. For 20 Hz ≤ Γ_e ≤ 1,100 Hz, we vary Γ_e for several fixed values of Γ_o and perform qubit readout measurements. The points are data from these measurements, and the dashed lines are a model using independently measured parameters of the electro-optic transducer. The model includes all sources of inefficiency such as loss, added noise and finite transduction bandwidth. All error bars represent one standard deviation.

apparatus can distinguish the coherent states encoding the state of the qubit, and can be characterized in situ by using the superconducting qubit as a non-Gaussian resource[25,34,35]. As measurement photons transit the cavity and extract information about the state of the qubit, the phase coherence of the qubit is necessarily destroyed[36]. This establishes a fundamental relationship between the signal-to-noise ratio of a dispersive measurement (Fig. 4a) and the measurement-induced dephasing owing to the qubit readout pulse[25] (Methods). An imperfect readout apparatus degrades the signal-to-noise ratio further, and thus reduction of the signal-to-noise ratio below this fundamental bound can be used to measure the loss and added noise of the readout process. We model the measurement apparatus as a beamsplitter with effective transmissivity η_q (top row in Fig. 4b), with an ideal optical heterodyne detector at the beamsplitter output, combining the effects of loss and added noise into a single performance metric (Methods).

In Fig. 4c, we measure the quantum efficiency while varying the electromechanical damping Γ_e for several different fixed values of the optomechanical damping rate Γ_o. For $\Gamma_e/\Gamma_o \ll 1$, the quantum efficiency is suppressed owing to mismatched damping rates[27], whereas the plateau in efficiency is primarily owing to noise emitted by the inductor-capacitor (LC) circuit and Γ_e-dependent LC circuit loss. From these measurements, we obtain a maximum quantum efficiency of $\eta_q \approx 8 \times 10^{-4}$. The dashed lines in Fig. 4c are obtained from a state-space model using measured transducer parameters (Supplementary Information).

To more directly compare the electro-optic transducer to existing results, we can instead describe the entire measurement apparatus as an effective amplifier with gain $\eta_{loss} = \eta_q/\eta_{noise}$ and two-quadrature added noise $N_t = \eta_{noise}^{-1} - 1$ at its output (Methods, bottom row in Fig. 4b), followed by an ideal optical heterodyne detector. Thus, the total noise at the input of the ideal optical heterodyne detector $N_{det} = 1 + N_t$ consists of the sum of the vacuum fluctuations, the added noise of this ideal heterodyne detector and the added noise of the transducer N_t.

We obtain a maximum transmission efficiency of $\eta_{loss} = 1.9 \times 10^{-3}$, which captures all sources of loss between the cQED system and the optical detector, and is more than two orders of magnitude larger than the best demonstrated efficiency for transduction of states from a superconducting qubit to the optical domain[9]. This maximum value of η_{loss} is the product of many individual contributions, and includes the transducer efficiency as defined in ref. [4] ($\eta_t = 0.19$), optical detection efficiency ($\eta_{opt} = 0.28$), microwave transmission loss ($\eta_{mic} = 0.34$) and inefficiency owing to the bandwidth of the readout pulse exceeding that of the transducer ($\eta_{bw} = 0.15$) (Methods). The noise at the input of the optical heterodyne detector is $N_{det} = 1 + N_t = 2.4$ photons at this operating point, owing primarily to technical noise emitted by the LC circuit, which is caused by the application of the strong microwave pump and is present even in the absence of laser light[27]. When calibrated using narrowband signals, the noise added at the input of the transducer is $N_{add} = 23$ photons, which is itself much larger than the minimum transducer added noise obtained at a different operating point[27].

However, with only moderate improvements in the bandwidth and added noise of the electro-optic transducer, the upconversion of non-trivial quantum states from a superconducting qubit is well within reach. Using standard techniques[22,37], the lifetime of the qubit in our cQED system can straightforwardly be improved to $T_1 > 100$ μs. Moreover, the vacuum electromechanical coupling g_e was smaller in this device than in previously measured transducers[4], suggesting that the transduction bandwidth can easily be improved to about 10 kHz by enhancing this coupling. The combination of spectrally narrower pulses emerging from the cQED system and increased g_e would remove bandwidth as a limiting factor, and enhancements in g_e would also reduce microwave noise by reducing the pump power required to achieve a given damping[27]. With $\Gamma_o = \Gamma_e = 2\pi \times 5$ kHz, $T_1 = 100$ μs and $N_t \ll 1$, we expect a quantum efficiency of $\eta_q \approx 0.1$ and the ability to transmit heralded quantum states from superconducting qubits exhibiting non-classical statistics. Two such systems would then enable remote entanglement of superconducting qubits over kilometre-scale distances.

Online content

Any methods, additional references, Nature Research reporting summaries, source data, extended data, supplementary information, acknowledgements, peer review information; details of author contributions and competing interests; and statements of data and code availability are available at https://doi.org/10.1038/s41586-022-04720-2.

1. Arute, F. et al. Quantum supremacy using a programmable superconducting processor. *Nature* **574**, 505–510 (2019).
2. Hisatomi, R. et al. Bidirectional conversion between microwave and light via ferromagnetic magnons. *Phys. Rev. B* **93**, 174427 (2016).
3. Han, J. et al. Coherent microwave-to-optical conversion via six-wave mixing in Rydberg atoms. *Phys. Rev. Lett.* **120**, 093201 (2018).
4. Higginbotham, A. P. et al. Harnessing electro-optic correlations in an efficient mechanical converter. *Nat. Phys.* **14**, 1038–1042 (2018).
5. Bartholomew, J. G. et al. On-chip coherent microwave-to-optical transduction mediated by ytterbium in YVO_4. *Nat. Commun.* **11**, 3266 (2020).

6. Arnold, G. et al. Converting microwave and telecom photons with a silicon photonic nanome- chanical interface. *Nat. Commun.* **11**, 4460 (2020).
7. Stockill, R. et al. Ultra-low-noise microwave to optics conversion in gallium phosphide. Preprint at https://arxiv.org/abs/2107.04433 (2021).
8. Sahu, R. et al. Quantum-enabled operation of a microwave-optical interface. *Nat. Commun.* **13**, 1276 (2022).
9. Mirhosseini, M., Sipahigil, A., Kalaee, M. & Painter, O. Superconducting qubit to optical photon transduction. *Nature* **588**, 599–603 (2020).
10. Barends, R. et al. Minimizing quasiparticle generation from stray infrared light in supercon-ducting quantum circuits. *Appl. Phys. Lett.* **99**, 113507 (2011).
11. Campbell, E. T. & Benjamin, S. C. Measurement-based entanglement under conditions of extreme photon loss. *Phys. Rev. Lett.* **101**, 130502 (2008).
12. Kalb, N. et al. Entanglement distillation between solid-state quantum network nodes. *Science* **356**, 928–932 (2017).
13. Zhong, C. et al. Proposal for heralded generation and detection of entangled microwave–optical-photon pairs. *Phys. Rev. Lett.* **124**, 010511 (2020).
14. Kurpiers, P. et al. Quantum communication with time-bin encoded microwave photons. *Phys. Rev. Appl.* **12**, 044067 (2019).
15. Hatridge, M. et al. Quantum back-action of an individual variable-strength measurement. *Science* **339**, 178–181 (2013).
16. Inagaki, T. et al. Entanglement distribution over 300 km of fiber. *Opt. Express* **21**, 23241 (2013).
17. Ursin, R. et al. Entanglement-based quantum communication over 144 km. *Nat. Phys.* **3**, 481–486 (2007).
18. Yin, J. et al. Satellite-based entanglement distribution over 1200 kilometers. *Science* **356**, 1140–1144 (2017).
19. Lecocq, F. et al. Control and readout of a superconducting qubit using a photonic link. *Nature* **591**, 575–579 (2021).
20. Youssefi, A. et al. A cryogenic electro-optic interconnect for superconducting devices. *Nat. Electron.* **4**, 326–332 (2021).
21. Zeuthen, E., Schliesser, A., Sørensen, A. S. & Taylor, J. M. Figures of merit for quantum transducers. *Quantum Sci. Technol.* **5**, 034009 (2020).
22. Reagor, M. et al. Quantum memory with millisecond coherence in circuit QED. *Phys. Rev. B* **94**, 014506 (2016).
23. Campagne-Ibarcq, P. et al. Quantum error correction of a qubit encoded in grid states of an oscillator. *Nature* **584**, 368–372 (2020).
24. Chakram, S. et al. Seamless high-Q microwave cavities for multimode circuit quantum elec-trodynamics. *Phys. Rev. Lett.* **127**, 107701 (2021).
25. Bultink, C. C. et al. General method for extracting the quantum efficiency of dispersive qubit readout in circuit QED. *Appl. Phys. Lett.* **112**, 092601 (2018).
26. Clerk, A. A. et al. Introduction to quantum noise, measurement, and amplification. *Rev. Mod. Phys.* **82**, 1155–1208 (2010).
27. Brubaker, B. M. et al. Optomechanical ground-state cooling in a continuous and efficient electro-optic transducer. Preprint at https://arxiv.org/abs/2112.13429 (2021).
28. Blais, A. et al. Cavity quantum electrodynamics for superconducting electrical circuits: An architecture for quantum computation. *Phys. Rev. A* **69**, 062320 (2004).
29. Gambetta, J. M. et al. Protocols for optimal readout of qubits using a continuous quantum nondemolition measurement. *Phys. Rev. A* **76**, 012325 (2007).
30. Caves, C. M. Quantum limits on noise in linear amplifiers. *Phys. Rev. D* **26**, 1817–1839 (1982).
31. Clerk, A. A. & Utami, D. W. Using a qubit to measure photon-number statistics of a driven thermal oscillator. *Phys. Rev. A* **75**, 042302 (2007).
32. Mallet, F. et al. Quantum state tomography of an itinerant squeezed microwave field. *Phys. Rev. Lett.* **106**, 220502 (2011).
33. Krantz, P. et al. A quantum engineer's guide to superconducting qubits. *Appl. Phys. Rev.* **6**, 021318 (2019).
34. Rosenthal, E. I. et al. Efficient and low-backaction quantum measurement using a chip-scale detector. *Phys. Rev. Lett.* **126**, 090503 (2021).
35. Touzard, S. et al. Gated conditional displacement readout of superconducting qubits. *Phys. Rev. Lett.* **122**, 080502 (2019).
36. Gambetta, J. M. et al. Qubit-photon interactions in a cavity: measurement-induced dephasing and number splitting. *Phys. Rev. A* **74**, 042318 (2006).
37. Place, A. P. M. et al. New material platform for superconducting transmon qubits with co-herence times exceeding 0.3 milliseconds. *Nat. Commun.* **12**, 1779 (2021).

Methods

cQED system

The cQED system consists of a planar superconducting transmon qubit coupled to the fundamental mode of a seamless 3D aluminium cavity. The qubit was fabricated on a 14 × 2 mm^2 *c*-plane sapphire chip. Using a single-electron-beam lithography step, the Dolan bridge process[38] was used to fabricate an Al–AlO_x–Al Josephson junction with area of 150 × 250 nm^2. The first layer of aluminium in the Al–AlO_x–Al structure was 30-nm thick and deposited via e-beam evaporation at an angle of 20°, which was then subsequently oxidized in 7 torr of pure oxygen for 3 min. Following formation of the aluminium oxide layer, a second layer of aluminium (60 nm) was deposited at an angle of −20°. The qubit capacitance comes from two rectangular 500 × 700 μm pads separated by 200 μm.

The cavity, a 40-mm-long circular waveguide with a radius of 4.7 mm, was machined out of a single piece of 99.999%-purity aluminium. The waveguide was open at one end, with a 7.25-mm-long post with a radius of 1.5 mm at the other end; this geometry defines the fundamental mode as a quarter-wave resonance with evanescent coupling to the waveguide above[22]. To reduce surface loss, the cavity was etched in Transene aluminium etchant type A for 24 h at ambient temperature.

A more unique feature of this cQED system is its tunability at the base temperature of the dilution refrigerator, which is enabled by the translation of a sapphire rod within the microwave cavity via a piezoelectric stepping module (Attocube ANPz101/LT/HV). This capability is required to bring the electro-optic transducer and cQED device into resonance at cryogenic temperatures. A sapphire rod with a radius of 2 mm is epoxied to a copper plate and fastened to the piezoelectric stepping module above the waveguide with a maximum travel of 5 mm. This assembly allows the sapphire rod to be translated along the centre of the waveguide to tune the fundamental mode's resonant frequency ω_c in situ by up to 1.7 GHz. The cavity mode has a total linewidth of $\kappa_c = \kappa_{c,w} + \kappa_{c,int} + \kappa_{c,ext} = 2\pi \times 380$ kHz, where $\kappa_{c,w}$, $\kappa_{c,ext}$, and $\kappa_{c,int}$ are the weakly coupled, strongly coupled and internal ports of the microwave cavity respectively. The cavity is strongly overcoupled to the transmission line connected to the electro-optic transducer such that $\kappa_{c,ext} \gg \kappa_{c,w}+\kappa_{c,int}$. See Extended Data Fig. 5 for a model of the cQED device alongside a photo of a representative cQED system (without the magnetic shielding).

The cQED system can be described by the Jaynes–Cummings model with interaction Hamiltonian $\hat{H}_{int}^{JC} = \hbar g_{qc}(\hat{d}^\dagger\hat{\sigma}^- + \hat{d}\hat{\sigma}^+)$, where g_{qc} is the qubit-cavity coupling rate and $\hbar$ is the reduced Planck constant. Here, the resonator has creation (annihilation) operator $\hat{d}^\dagger$ ($\hat{d}$), and can swap excitations with the qubit via the raising (+) and lowering (−) operators $\hat{\sigma}_\pm$. When the qubit-resonator detuning $\Delta_{qc} = \omega_q - \omega_c$ is large such that $g_{qc} \ll |\Delta_{qc}|$, the Jaynes–Cummings model can be described under the dispersive approximation $\hat{H}_{int}^{JC} = -\hbar\chi\hat{\sigma}_z\hat{d}^\dagger\hat{d}$. The dispersive shift χ is given by $\chi = g_{qc}^2\nu/(\Delta_{qc}(\Delta_{qc}-\nu))$[39], where the qubit anharmonicity ν encodes the contribution from higher-energy levels of the transmon qubit. See Extended Data Table 1 for a list of parameters describing the cQED system.

The qubit lifetime ($T_1 = 17$ μs) is far from Purcell limited[40], probably owing to participation of lossy dielectrics that remain after e-beam lithography and aluminium deposition. The coherence time of the qubit is $T_2^R \approx T_2^{echo} \approx 20$ μs, and no difference is seen when it is measured using a Hahn echo versus a standard Ramsey sequence.

The cQED system is contained in a magnetic shield comprising an outer shield of high-permeability Amumetal 4K and an inner shield made of pure aluminium to minimize stray magnetic fields near the cQED system during cooling of the device through its critical temperature.

Electro-optic transducer

The electro-optic transducer consists of a microwave resonator and an optical resonator coupled to a single mode of a micromechanical oscillator. It is described by the Hamiltonian

$$\frac{\hat{H}}{\hbar} = \omega_o\hat{a}^\dagger\hat{a} + \omega_e\hat{b}^\dagger\hat{b} + \omega_m\hat{c}^\dagger\hat{c} + (g_o\hat{a}^\dagger\hat{a} + g_e\hat{b}^\dagger\hat{b})(\hat{c}+\hat{c}^\dagger), \quad (2)$$

where $\hat{a}$, $\hat{b}$ and $\hat{c}$ are the annihilation operators for the optical, microwave and mechanical modes, respectively, and g_o (g_e) is the vacuum optomechanical (electromechanical) coupling rate.

The mechanical oscillator is a 100-nm-thick, 500-μm-wide-square silicon-nitride membrane suspended from a silicon chip. Phononic shielding with a bandgap centred around $\omega_m = 2\pi \times 1.45$ MHz is patterned into the silicon chip, isolating the membrane mode used for transduction from the vibrational modes of the chip. The phononic shield uses few unit cells to maintain a reasonably sized flip chip for integration with the electro-optic transducer. This shielding results in a quality factor $Q_m = 1.3 \times 10^7$ for the mode of interest, or equivalently an energy dissipation rate $\gamma_m = 2\pi \times 0.11$ Hz.

The microwave resonator is a superconducting flip-chip LC circuit whose capacitance is modulated by the motion of a superconducting pad deposited on the membrane. The vacuum electromechanical coupling is determined by the distance d between this pad and a second capacitor pad on a separate nearby chip hosting the rest of the circuit, which is $d \approx 300$ nm for most devices. In the transducer used in this work, the capacitor pad separation was unusually large, probably owing to thermal contraction of the epoxy (Stycast 2850) that was used to attach the chips to each other. This resulted in a lower vacuum electromechanical coupling rate than in previous devices[4]:

$$g_e = p\frac{\omega_e}{2d} = 2\pi \times 1.6 \text{ Hz}, \quad (3)$$

where $p = 0.67$ is the participation ratio of the motional capacitance in ω_e, and $d = 830$ nm (ref. [27]). Wafer bonding without the use of epoxy is being explored to couple the two chips together and enable smaller plate separation d and hence larger g_e. The LC circuit is coupled via mutual inductance[27] to a microwave transmission line at rate $\kappa_{e,int} = 2\pi \times 1.42$ MHz, and its total linewidth κ_e varies between 1.6 MHz and 2.7 MHz owing to the dependence of the internal loss $\kappa_{e,int}$ on the power of the microwave pump used to mediate transduction.

The optical resonator is a Fabry–Pérot cavity defined by high-reflectivity ion-beam-sputtered mirror coatings deposited by FiveNine Optics, which are chosen to be very asymmetric such that the cavity mode couples preferentially out the front mirror with external coupling $\kappa_{o,ext} = 2\pi \times 2.12$ MHz. The total cavity linewidth is $\kappa_o = \kappa_{o,ext} + \kappa_{o,int} = 2\pi \times 2.68$ MHz, where $\kappa_{o,int}$ includes scattering and absorption losses as well as transmission through the back mirror. The membrane is positioned at a maximum in the intensity gradient of the intracavity light, yielding a vacuum coupling rate $g_o = 2\pi \times 60$ Hz. The heterodyne mode matching factor quantifying the overlap of the propagating optical cavity mode and the local oscillator (LO) beam is $\varepsilon = 0.80$.

During operation, strong optical and microwave pumps are applied near the corresponding electromagnetic resonances to enhance the vacuum coupling rates g_o and g_e, respectively[41]. Transforming to a rotating frame to remove the free evolution of the fields, $\hat{a} \to \hat{a}e^{-i\omega_o t}$, $\hat{b} \to \hat{b}e^{-i\omega_e t}$ and $\hat{c} \to \hat{c}e^{-i\omega_m t}$, the Hamiltonian can then be linearized around the strong pumps to yield

$$\frac{\hat{H}_{int}^{lin}}{\hbar} = g_o\bar{a}(\hat{a}^\dagger + \hat{a})(\hat{c}+\hat{c}^\dagger) + g_e\bar{b}(\hat{b}^\dagger + \hat{b})(\hat{c}+\hat{c}^\dagger), \quad (4)$$

where $\bar{a}$ ($\bar{b}$) is the optical (microwave) mode coherent state amplitude due to the incident pump. Both pumps are red-detuned from the respective resonances by ω_m, resonantly enhancing the optomechanical and electromechanical beamsplitter terms in the Hamiltonian[42]. In the resolved sideband limit at this optimal detuning, the optomechanical

(electromechanical) damping rate is then given by $\Gamma_o = 4g_o^2\bar{a}^2/\kappa_o$ ($\Gamma_e = 4g_e^2\bar{b}^2/\kappa_e$). The transducer bandwidth is given by $\Gamma_T = \Gamma_e + \Gamma_o + \gamma_m$.

The electro-optic transducer parameters are summarized in Extended Data Table 1. See ref. [27] for a more detailed description of the fabrication, assembly and characterization of the electro-optic transducer, as well as the theory of transducer operation.

Experimental layout

A schematic of the experimental setup is shown in Extended Data Fig. 4. Here we briefly summarize the details of the optical setup, discussed further in ref. [27].

The 1,084-nm laser light used for optical detection is supplied by a widely tunable external cavity diode laser (Toptica Photonics CTL 1050), and is split into three separate beams whose frequencies are shifted relative to one another by acousto-optic modulators (not shown). The lock beam (yellow) is nearly resonant with a TEM_{00} mode of the optical cavity (detuned by approximately −50 kHz), and is used to stabilize the beam frequencies relative to the optical cavity resonance frequency with the Pound–Drever–Hall technique. The optical pump beam (red) is detuned from cavity resonance by $-\omega_m$. The LO beam (maroon) is detuned from the pump beam by −12.9 MHz. The reflected pump beam (including the transduced measurement pulse) is interfered with the LO beam on a balanced photodetector (Thorlabs PDB450C) for heterodyne detection. The resulting signal is demodulated using a Zurich Instruments HF2LI lock-in amplifier, whose output is recorded with an AlazarTech ATS9462 digitizer.

As shown in Extended Data Fig. 4, the qubit control and readout pulses are generated via individual sources (Agilent E8257D and N5172B). For the qubit drive pulses and readout pulses, these generators emit a continuous signal centred at the frequencies ω_d and ω_c, respectively. To control the envelope of each pulse, the signals are gated by inphase/quadrature (IQ) mixers or double balanced mixers, while fast microwave switches are placed at the output of each mixer to prevent leakage of the LO through the mixer when the signals are supposed to be turned off. For measurement-induced dephasing experiments (Extended Data Fig. 3), the readout signal is split and run through a separate mixer and switch to enable individual control of the readout and weak measurement pulses (Extended Data Fig. 4a). An arbitrary waveform generator (Zurich instruments HDAWG) controls the timing and envelope of the pulses, and triggers the digitizers used to capture both the optical and microwave readout signals (AlazarTech ATS9462).

Superconducting qubit readout signal-to-noise ratio

In a dispersive measurement, a coherent state $|\alpha\rangle$ is entangled with the state of the qubit. If initially the qubit is prepared in a superposition state $|\psi_q\rangle = \frac{1}{\sqrt{2}}(|e\rangle + |g\rangle)$, its interaction with the driven cavity mode causes it to evolve into the state

$$|\psi_m\rangle = \frac{1}{\sqrt{2}}(|e\rangle|\alpha_e\rangle + |g\rangle|\alpha_g\rangle), \tag{5}$$

where $|\alpha_e\rangle$ and $|\alpha_g\rangle$ are coherent states with equal magnitude but phases shifted by $\theta_\pm = \pm \arctan 2\chi/\kappa_c$, with the + (−) sign corresponding to the qubit in $|g\rangle$ ($|e\rangle$). The readout amplitude $\sqrt{\bar{n}_r} = |\alpha|\sin\theta$ determines the separation in phase space between these two coherent states. The degree to which we can resolve the two Gaussian distributions in phase space is quantified by the signal-to-noise ratio (SNR): loss degrades the SNR by reducing the phase space separation, whereas noise degrades the SNR by increasing the variance of each distribution. We define the SNR as

$$\mathrm{SNR} = \frac{|\mu_e - \mu_g|}{\sigma_{ge}}, \tag{6}$$

where $\sigma_{ge} = \sigma_e = \sigma_g$ is the standard deviation of the Gaussian-distributed optical heterodyne voltage corresponding to the qubit in either the ground or the excited state, and μ_g and μ_e are the mean values of the two distributions. Noise N_t gets added by the transducer, and some of the signal is lost such that $|\alpha| \to \eta_{loss}|\alpha|$; thus the SNR can be written as

$$\mathrm{SNR} = \frac{2\sqrt{2}\eta_{loss}|\alpha|\sin\theta}{\sqrt{1+N_t}}. \tag{7}$$

Measurement-induced dephasing and the quantum efficiency

Reading out the state of the qubit through the cavity necessarily causes fluctuations in the frequency of the qubit owing to the dispersive interaction between the qubit and the cavity $H_{int} = -\chi\hat{\sigma}_z\hat{d}^\dagger\hat{d}$. This leads to measurement-induced dephasing[36], destroying the coherence of any initial superposition. The off-diagonal elements of the qubit's density matrix after this interaction are given by $\rho_{ge} = \rho_{ge}(0)e^{-2|\alpha|^2\sin^2(\theta)} = e^{-2\bar{n}_r}$ (ref. [34]).

To demonstrate measurement-induced dephasing, we inject a weak measurement pulse into a Ramsey sequence (Extended Data Fig. 1a), and measure the resulting amplitude of the Ramsey oscillations—where $\rho_{ge} = \langle\hat{\sigma}_z\rangle/4$—using a strong projective measurement of the qubit. Extended Data Fig. 1b shows the results of these measurements, using the microwave readout chain and varying the strength of the weak 15-μs readout pulse. We observe a clear Gaussian decay of ρ_{ge} as a function of readout amplitude $\sqrt{\bar{n}_r}$.

This measurement-induced dephasing quantifies the amplitude of the readout pulse inside the cQED system's microwave cavity, whereas the SNR quantifies the distinguishability of the two (thermal) coherent states at the optical detector. Thus, these two quantities are fundamentally related to each other through the quantum efficiency $\eta_q = \frac{\eta_{loss}}{1+N_t}$ (ref. [25]), which describes the optical measurement apparatus as an effective beamsplitter between the cQED system and an ideal optical heterodyne detector.

Technical details of the quantum efficiency calibration

To control the readout amplitude $\sqrt{\bar{n}_r}$, a drive voltage V is varied via an IQ mixer. The SNR and Gaussian decay of ρ_{ge} can be recast in terms of this drive voltage as: $\mathrm{SNR} = aV$ and $\rho_{ge} = \rho_{ge}(0)e^{-\frac{V^2}{2\sigma^2}}$. As shown in ref. [25], the quantum efficiency is then a function of the slope of the SNR a (Extended Data Fig. 1c) and the width of the Gaussian distribution σ:

$$\eta_q = \frac{\sigma^2 a^2}{2}, \tag{8}$$

where in this convention an ideal heterodyne detector would have $\eta_q = 1$

Contributions to the quantum efficiency

The quantum efficiency of the electro-optic qubit readout apparatus can be split into seven main components, $\eta_q = \eta_{bw}\eta_t\eta_G\eta_{mic}\eta_{opt}\eta_{cav}\eta_{noise}$. We describe each contribution below, and the contributions are also summarized in Extended Data Table 2.

Bandwidth limitations. A significant contribution to η_q is due to the mismatch in bandwidth between the transducer and the readout pulse emitted by the qubit cavity. In the rotating-wave approximation, and approximating the cQED system's output as a square pulse with width T_p, we obtain

$$\eta_{bw} \approx 1 - 2\frac{(1 - e^{-\Gamma_T T_p/2})}{\Gamma_T T_p}. \tag{9}$$

Solving for the full dynamics without the above approximations gives a contribution to the efficiency in the range $0.02 < \eta_{bw} < 0.15$ over the range of Γ_T values plotted in Fig. 4c.

Transducer efficiency. The relatively low electromechanical coupling in this device ($g_e = 2\pi \times 1.6$ Hz) limits the maximum achievable

electromechanical damping rate to $\Gamma_e = 2\pi \times 1.1$ kHz. To maximize the bandwidth, we often operate the transducer in a mismatched mode with $\Gamma_o \gg \Gamma_e$, but this comes at a cost to the narrowband signal efficiency of the transducer[27]:

$$\eta_t = \varepsilon \frac{\kappa_{o,ext}}{\kappa_o} \frac{\kappa_{e,ext}}{\kappa_e} \frac{4\Gamma_e \Gamma_o}{\Gamma_T^2}, \quad (10)$$

where ε is the optical cavity mode matching. This sets an upper bound on the efficiency with which broadband signals can be transduced. Equation (10) also depends on Γ_e implicitly owing to the pump-power-dependent LC circuit loss[27]. This contribution is responsible for the sharp drop in efficiency for $\Gamma_e \ll \Gamma_o$ on each curve in Fig. 4c, and contributes to the plateau in η_q at high Γ_e for each fixed value of Γ_o.

Transducer gain. Owing to the finite sideband resolution of the electro-optic system[42], the transducer has gain[41]

$$\eta_G = \left(1 + \left(\frac{\kappa_e}{4\omega_m}\right)^2\right)\left(1 + \left(\frac{\kappa_o}{4\omega_m}\right)^2\right). \quad (11)$$

This two-quadrature gain is undesirable for transduction, as it is necessarily accompanied by unwanted added noise[30], but it is a small effect, varying in the range $1.3 < \eta_G < 1.5$ with microwave pump power.

Microwave transmission loss between the cQED system and the transducer. Our system also permits qubit readout through a microwave readout apparatus, shown in Fig. 1b. Its quantum efficiency η_q^{mic} is defined to include all sources of loss and noise that affect the readout pulse as it emerges from the cQED system's cavity, reflects off the transducer's LC circuit, and is detected using the microwave heterodyne measurement chain. Measuring η_q^{mic} allows us to back out the microwave transmission loss η_{mic} between the cQED system and the transducer, which also contributes to η_q. As shown in Extended Data Fig. 2, η_q^{mic} decreases significantly with increasing Γ_e—mainly owing to Γ_e-dependent reflection loss. These data are fit to a model (purple curve in Extended Data Fig. 2) that includes the effects of Γ_e-dependent LC circuit reflection loss, noise emitted from the microwave port of the transducer, and independently calibrated microwave measurement chain added noise referred to the transducer output[27], with η_{mic} as the only free parameter, yielding $\eta_{mic} = 0.34$ (4.7 dB). This relatively high loss can be mitigated by reducing the total number of microwave connectors in the signal path, switching to superconducting cables, and removing filters from the signal path and placing them instead on the pump and cancellation lines.

Using the quantum efficiency of the optical measurement apparatus and a state-space model (Supplementary Information), we perform a fit to η_q as $\Gamma_e + \Gamma_o$ is varied, with η_{mic} as the only free parameter. This yields an apparent microwave loss of $\eta_{mic}^{app} = 0.17$, in slight tension with $\eta_{mic} = 0.34$ inferred from the microwave measurement described above. This discrepancy may be owing to drifts in the optical cavity mode matching or microwave chain gain over a timescale of several months.

Optical detection efficiency. The optical detection efficiency is given by the product of factors encoding optical transmission losses between the transducer and the balanced heterodyne detector, the inefficiency of the heterodyne detector itself, and the detector's dark noise: together these three factors yield $\eta_{opt} = 0.28$. This figure excludes optical cavity losses and imperfect mode matching, which are included in the transducer efficiency, equation (10).

cQED system cavity loss. Through the measured attenuation on the lines, we bound the sum of the of the weak port coupling and the internal loss to $\kappa_{c,int} + \kappa_{c,w} < 2\pi \times 15$ kHz. Thus $\eta_{cav} = 1 - \frac{\kappa_{c,int} + \kappa_{c,w}}{\kappa_c} > 0.96$ does not significantly affect η_q.

Added noise. Here we show how the noise measured at the input of the optical heterodyne detector, or equivalently at the output of an effective amplifier with gain η_{loss}, can alternatively be expressed as a contribution to the quantum efficiency η_q of the electro-optic readout apparatus, modelled as an effective beamsplitter (Fig. 4b).

The voltage records obtained from optical heterodyne detection of the upconverted qubit readout pulse can be written in the form

$$I_{|k\rangle}(t) = \sqrt{G_o}\left(\sqrt{\kappa_c \eta_{loss}}\,\mathrm{Re}(\alpha_{|k\rangle}(t)) + \hat{\zeta}_I(t)\right) \quad (12)$$

$$Q_{|k\rangle}(t) = \sqrt{G_o}\left(\sqrt{\kappa_c \eta_{loss}}\,\mathrm{Im}(\alpha_{|k\rangle}(t)) + \hat{\zeta}_Q(t)\right), \quad (13)$$

where $\sqrt{G_o}$ is an overall gain factor and the index $k = \{g, e\}$ labels whether the qubit was prepared in the ground state or the excited state. $\eta_{loss} = \eta_{bw}\eta_t\eta_G\eta_{mic}\eta_{opt}\eta_{cav}$ includes all sources of loss between the cQED system and the ideal optical detector, and $\hat{\zeta}_I$ and $\hat{\zeta}_Q$ are noise operators whose autocorrelation functions include contributions from vacuum fluctuations, the added noise of an ideal heterodyne detector and transducer added noise N_t:

$$\langle\hat{\zeta}_I(t)\hat{\zeta}_I(t')\rangle = \langle\hat{\zeta}_Q(t)\hat{\zeta}_Q(t')\rangle = \frac{1}{2}(1 + N_t)\delta(t - t'). \quad (14)$$

Equations (12)–(14) define the amplifier model described in Fig. 4b in which the transduction process is characterized by an efficiency η_{loss} and total two-quadrature noise $N_{det} = 1 + N_t$ at the input of an ideal optical detector. However, for qubit readout, it is often more convenient to combine these metrics into a single figure of merit. To this end, we rescale equations (12), (13) to obtain

$$I(t) = \sqrt{G_o'}\left(\sqrt{\frac{\kappa_c \eta_{loss}}{1 + N_t}}\,\mathrm{Re}(\alpha_{|k\rangle}(t)) + \tilde{\zeta}_I(t)\right) \quad (15)$$

$$Q(t) = \sqrt{G_o'}\left(\sqrt{\frac{\kappa_c \eta_{loss}}{1 + N_t}}\,\mathrm{Im}(\alpha_{|k\rangle}(t)) + \tilde{\zeta}_Q(t)\right), \quad (16)$$

where $\sqrt{G_o'} = \sqrt{G_o(1 + N_t)}$ is a modified overall gain factor, and $\tilde{\zeta}_I$ and $\tilde{\zeta}_Q$ are noise operators containing only contributions from vacuum fluctuations and ideal heterodyne detection: $\langle\tilde{\zeta}_I(t)\tilde{\zeta}_I(t')\rangle = \langle\tilde{\zeta}_Q(t)\tilde{\zeta}_Q(t')\rangle = \frac{1}{2}\delta(t - t')$. From equations (15), (16) it is clear that η_q can be defined as

$$\eta_q = \eta_{loss}\eta_{noise} = \eta_{loss} \times \frac{1}{1 + N_t}. \quad (17)$$

See Supplementary Information for a derivation of the exact form of N_t.

Prospects for quantum transduction

The relevant figure of merit for quantum-state transduction is the added noise referred to the output of the cQED system $N_{cQED} = N_t/\eta_{loss}$ (ref. [21]). When we optimize for maximum efficiency, with $(\Gamma_e, \Gamma_o)/2\pi = (1.1, 5.0)$ kHz, and achieve $\eta_q \approx 8 \times 10^{-4}$, we obtain $N_{cQED} = 740$ photons. This is, of course, far from the value required for quantum-enabled transduction[21] and is limited by insufficient bandwidth, LC circuit loss, transducer efficiency and pump-power-dependent noise generated by the LC circuit[27]. However, even moderate improvements in the vacuum electromechanical coupling g_e will greatly improve η_{bw}, η_t and η_{noise}.

An increase in g_e would provide many simultaneous improvements to the operation of the transducer by reducing the number of microwave pump photons required to achieve a given transduction bandwidth.

For example, $g_e = 2\pi \times 8$ Hz would enable $\Gamma_e = \Gamma_o = 2\pi \times 5$ kHz and reduce pump-power-dependent LC circuit loss, yielding $\eta_t \approx 0.6$. If accompanied by an increase in the qubit decay times to $T_2 = T_1 = 100$ μs, we expect $\eta_{bw} = 0.9$, and the transducer to be quite close to quantum-enabled with $N_{cQED} < 10$. Further reductions in added noise, which will be needed to approach the $N_{cQED} < 1$ regime, are currently being explored, including the use of wafer bonding to achieve more reliable and even larger electromechanical coupling rates. Pump-induced vortex loss in the superconductor is also currently being investigated as a possible source of both LC circuit loss and added noise, which may be improved through better magnetic shielding.

Isolation and filtering

The two modular systems are connected via a coaxial transmission line through a single-junction circulator in series with a triple-junction circulator. This provides a total of 63 dB of isolation to shield the cQED system from the strong microwave pump (up to −45 dBm incident on the LC circuit), which is routed to the transducer through a directional coupler. Additional isolation is achieved by sending a cancellation tone through the second port of the directional coupler (labelled 'cancel port' in Extended Data Fig. 3a) to interferometrically cancel the large reflected microwave pump[32]. Filters are also placed between the cQED system and the transducer to eliminate the propagation of high-frequency thermal radiation along the coaxial cable connecting the two systems. See Extended Data Fig. 4c for details of the layout and filtering.

Source of excess backaction

As shown in Fig. 3b, there is a small amount of excess backaction from the operation of the transducer at very high Γ_e, equivalent to $\Delta n = (3 \pm 1) \times 10^{-3}$ excess photons in the cQED system's microwave cavity. This excess backaction is inferred from measurements of the pure dephasing time of the qubit $T_\phi^{-1} = T_2^{-1} - \frac{1}{2}T_1^{-1}$—see Extended Data Fig. 6—using equation (1). Two possible mechanisms could cause such excess backaction: heating of the 50-Ω termination that thermalizes the cQED system by the strong microwave pump, or direct backaction from pump photons making it through the isolation between the cQED system and the transducer. We can differentiate these two possible sources of backaction by using our cancellation scheme as an interferometer to tune the power P_{ref} of the microwave field propagating towards the cQED system (Extended Data Fig. 3a, b).

The number $\bar{n}_p$ of pump photons in the cQED system's microwave cavity can be accurately measured by monitoring the qubit frequency shift $\Delta\omega_q = 2\chi\bar{n}_p$ due to the (coherent) a.c. Stark effect[36]. Extended Data Fig. 3c shows the number of coherent pump photons in the cQED system's cavity as a function of P_{ref}. During normal operation of the transducer, the cancellation is optimized so that $P_{ref} < -95$ dBm, and we can linearly extrapolate $\bar{n}_p$ to low powers to find that $\bar{n}_p < 1 \times 10^{-3}$ during normal operation. The measured excess backaction $\Delta n = (3 \pm 1) \times 10^{-3}$ is larger, so it is likely that local heating of the 50-Ω termination that thermalizes the cQED system is responsible for the majority of the excess backaction observed in Fig. 3b. Improvements in g_e that will enable a reduction in microwave pump power should further reduce this excess backaction.

Importance of backaction for remote entanglement protocols

As optical fibre imposes photon loss of at least 0.14 dB km^{-1} (ref. [43]), encodings with fidelity insensitive to photon loss are required for optical quantum networks. A recently proposed and promising example of a protocol that heralds quantum states in such a manner uses time-bin qubits of the form $|\psi\rangle = \alpha|t_a\rangle + \beta|t_b\rangle$, where t_a and t_b represent two distinguishable arrival times for a single photon. There are different techniques for generating such superpositions[14], but two temporally separated gates are required to transmit the qubit. This describes a protocol for transmitting heralded quantum states through a lossy quantum network.

However, if the process of transducing the single photon disrupts the circuit QED system generating the time-bin qubit, then turning on the electro-optic transducer during the first time bin will destroy the entire time-bin qubit and prevent the transmission of any quantum information. More broadly, any quantum communication protocol that requires a qubit gate operation after the electro-optic transducer has been turned on requires that the electro-optic transducer not disrupt the state of the qubit.

Data availability

The data and code supporting the figures are available on Zenodo at https://doi.org/10.5281/zenodo.6344913. Source data are provided with this paper.

38. Dolan, G. J. Offset masks for lift-off photoprocessing. *Appl. Phys. Lett.* **31**, 337–339 (1977).
39. Koch, J. et al. Charge-insensitive qubit design derived from the Cooper pair box. *Phys. Rev. A* **76**, 042319 (2007).
40. Houck, A. A. et al. Controlling the spontaneous emission of a superconducting transmon qubit. *Phys. Rev. Lett.* **101**, 080502 (2008).
41. Andrews, R. W. et al. Bidirectional and efficient conversion between microwave and optical light. *Nat. Phys.* **10**, 321–326 (2014).
42. Aspelmeyer, M., Kippenberg, T. J. & Marquardt, F. Cavity optomechanics. *Rev. Mod. Phys.* **86**, 1391–1452 (2014).
43. Tamura, Y. et al. The first 0.14-db/km loss optical fiber and its impact on submarine transmission. *J. Lightwave Technol.* **36**, 44–49 (2018).

Acknowledgements We acknowledge funding from AFOSR MURI grant number FA9550-15-1-0015, from ARO CQTS grant number 67C1098620 and the NSF under grant number PHYS 1734006. We thank J. Beall and K. Cicak for help with our fabrication process. We thank J. Teufel, G. Smith, K. Quinlan, K. Adachi and L. Talamo for feedback on the manuscript.

Author contributions R.D.D., C.A.R. and K.W.L. conceived the experiment. B.M.B., M.D.U., J.M.K., S.M. and R.D.D. planned and carried out the measurements. M.D.U. constructed the optical cavity. R.D.D. designed and fabricated the cQED system. S.M. and P.S.B. developed the fabrication process for the chips hosting the electrical circuit and membrane, which were fabricated by S.M. All authors contributed to writing the manuscript.

Competing interests The authors declare no competing interests.

Additional information

Supplementary information The online version contains supplementary material available at https://doi.org/10.1038/s41586-022-04720-2.

Correspondence and requests for materials should be addressed to R. D. Delaney.

Peer review information *Nature* thanks Wolfgang Pfaff, Gary Steele and the other, anonymous, reviewer(s) for their contribution to the peer review of this work. Peer reviewer reports are available.

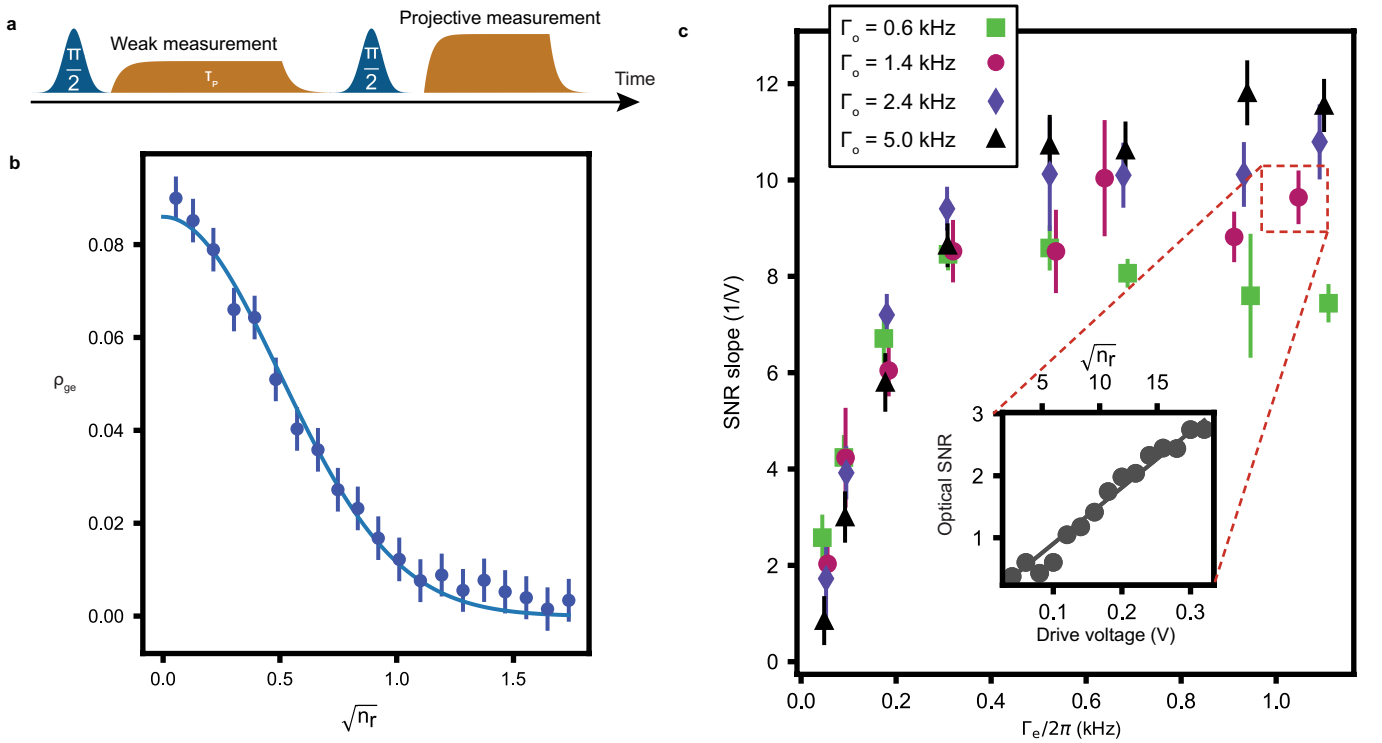

Extended Data Fig. 1 | Quantum efficiency measurement. (a) Protocol for measurement-induced dephasing calibration. A weak measurement pulse is injected into a Ramsey sequence. The Ramsey sequence is then followed by a strong projective measurement of the qubit. (b) The coherence of the qubit ρ_{ge} decays as a Gaussian function of the weak measurement amplitude $\sqrt{\bar{n}_r}$. The points are data, while the line is a Gaussian fit. (c) Measurement of the SNR slope a of the electro-optic readout, in units of inverse drive voltage, as a function of Γ_e for four fixed optomechanical damping rates Γ_o. Each data point is obtained from a fit to a measurement of the sort shown in the inset, where it is seen that the SNR scales linearly as a function of drive voltage (bottom axis) or equivalently readout pulse amplitude (top axis).

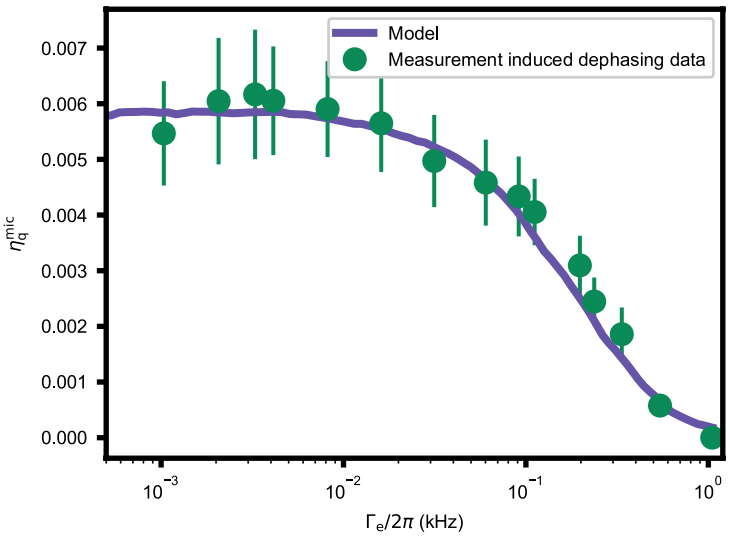

Extended Data Fig. 2 | Characterisation of the quantum efficiency of the microwave readout apparatus. The microwave readout efficiency η_q^{mic} is measured as a function of the electromechanical damping rate Γ_e. The points are data, while the line is a model including partial absorption of the readout pulse by the pump power-dependent reflection loss of the LC circuit, power-dependent added noise, fixed transmission losses and the independently measured added noise of the microwave heterodyne measurement chain. The shape of the curve is dominated by power-dependent LC circuit reflection loss, with the quantum efficiency of the microwave readout apparatus approaching zero at high power because the LC circuit is nearly critically coupled. From this model, we estimate 4.7 dB of loss ($\eta_{mic} = 0.34$) between transducer and the cQED system.

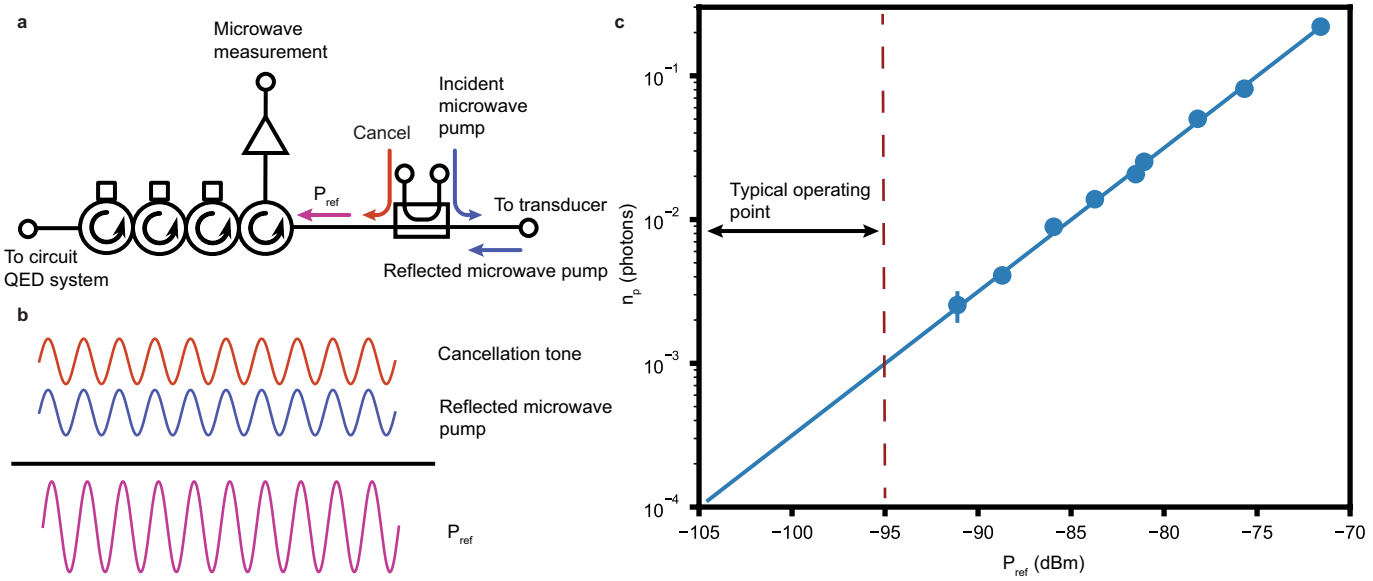

Extended Data Fig. 3 | Excess backaction from pump photon leakage. (a) Circulators (total isolation of 63 dB) and interferometric cancellation are used to prevent the strong microwave pump from reaching the cQED system and dephasing the qubit. Cancellation is achieved by sending a microwave cancellation tone with amplitude equal to that of the reflected microwave pump but opposite phase into the second arm of the directional coupler. The phasor sum of this cancellation tone and the reflected microwave pump determines the pump power P_{ref} propagating towards the cQED system. (b) The directional coupler acts as an interferometer, enabling interference between the reflected microwave pump and the cancellation tone. During normal operation of the transducer the cancellation tone is tuned to minimise P_{ref}, but to estimate the effect of pump photons on the qubit the cancellation tone can be tuned to only partially interfere and tune P_{ref} over several decades. The phasor sum shown here is for the case of constructive interference. (c) The number of pump photons in the cQED system $\bar{n}_p$ is measured as P_{ref} is varied. During transducer operation the cancellation is typically tuned to achieve $P_{ref} < -95$ dBm or equivalently $\bar{n}_p < 1 \times 10^{-3}$. The cancellation does not stay completely fixed over the course of the experiment due to small thermal drifts slightly changing the amplitude of P_{ref}.

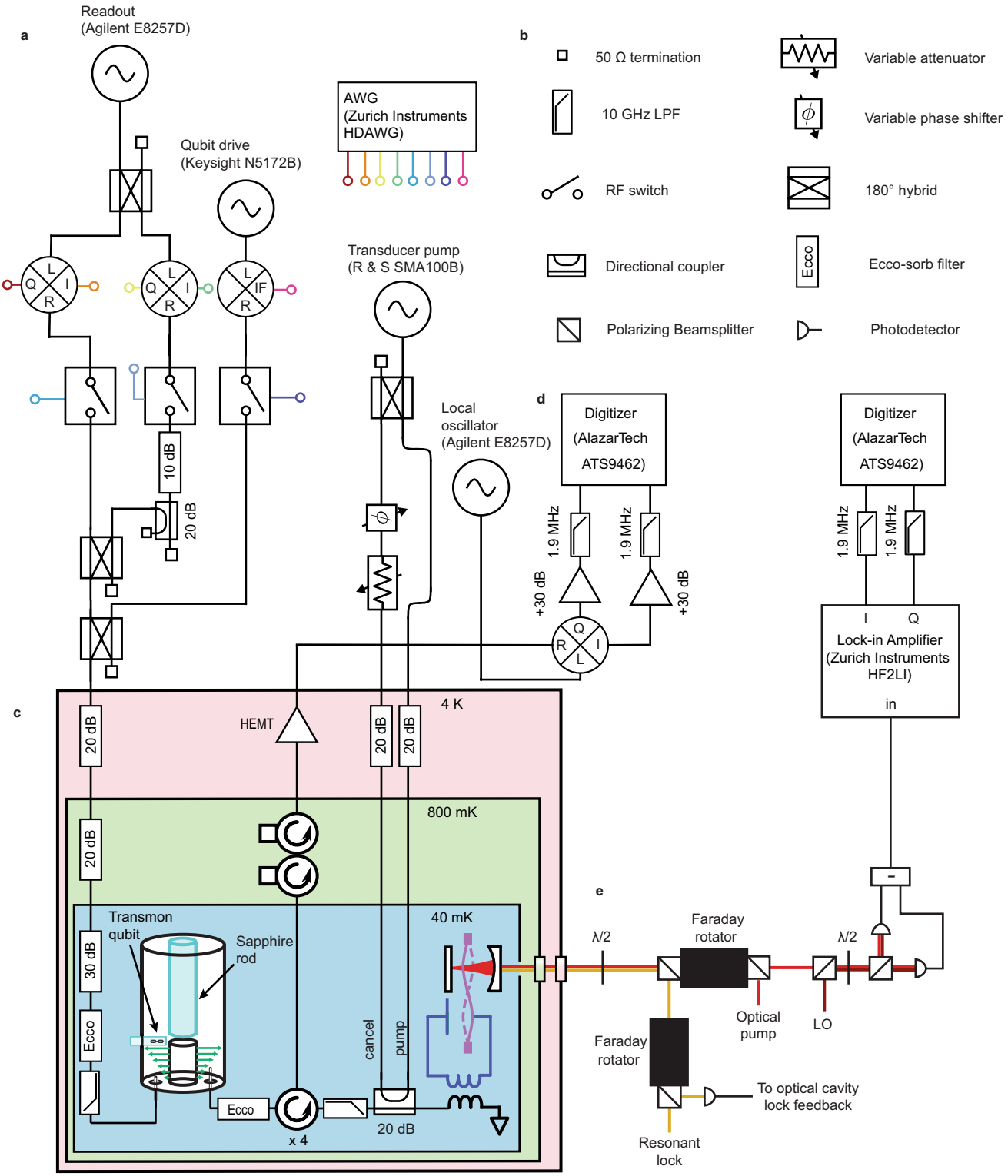

Extended Data Fig. 4 | Experimental schematic. (a) Microwave layout demonstrating the exact configuration of the qubit readout/control pulses and the pumps for the electro-optic transducer. (b) Legend for various different microwave and optical components. (c) Cryogenic portion of the experiment. (d) Demodulation and detection scheme. The two digitisers allow for simultaneous measurement of the microwave and optical signals emitted from the transducer. (e) Simplified schematic of optical beam layout and balanced heterodyne detector.

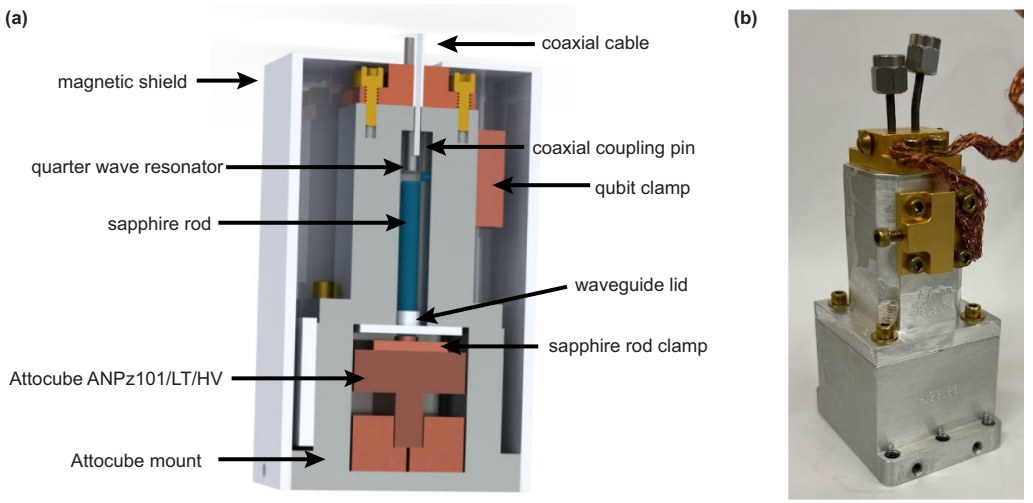

Extended Data Fig. 5 | cQED system. (a) The cQED system is a superconducting qubit coupled to a 3D quarter-wave post resonator which is in turn evanescently coupled to the waveguide above. A sapphire rod can be translated towards the end of the post resonator via a piezo-electric stepping module (Attocube ANPz101/LT/HV) in order to tune the resonator's frequency. The sapphire rod is epoxied to a clamp with stycast 2850 and then bolted to the piezo-electric stepping module. A lid with a narrow hole for the sapphire rod to pass through is attached to the top of the waveguide to prevent coupling of modes in the Attocube mount to modes within the waveguide and the quarter-wave resonator. (b) Photo of the cQED system and Attocube mount. A copper braid is attached to the gold-plated copper qubit clamp to help thermalize the superconducting qubit.

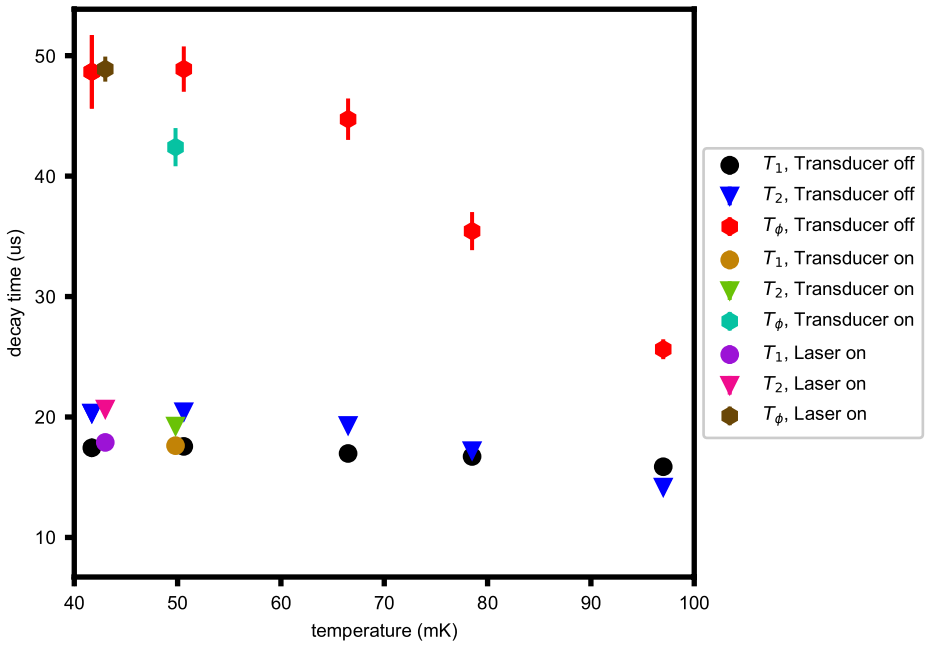

Extended Data Fig. 6 | Qubit coherence time data. Qubit coherence times under three different electro-optic transducer operating conditions: transducer off, transducer on with $(\Gamma_e, \Gamma_o)/2\pi = (1.1, 5.0)$ kHz and just the laser on with $(\Gamma_e, \Gamma_o)/2\pi = (0, 5.0)$ kHz. Turning just the laser on is indistinguishable from the transducer being turned off. Running the electro-optic transducer does reduce the dephasing time of the qubit (see the cyan hexagon). Circles represent T_1 times, triangles represent T_2 times and hexagons represent T_ϕ.

Extended Data Table 1 | cQED system and electro-optic transducer parameters

Parameter	Symbol	Value
Qubit frequency	ω_q	$\omega_q/2\pi = 5.632$ GHz
Qubit-cavity coupling	g_{qc}	$g_{qc}/2\pi = 66.4$ MHz
Qubit anharmonicity	v	$v/2\pi = 228$ MHz
Dispersive shift	χ	$\chi/2\pi = 172$ kHz
Critical photon number	n_{crit}	$n_{crit} = 302$ photons
Cavity frequency	ω_c	$\omega_c/2\pi = 7.938$ GHz
Cavity linewidth	κ_c	$\kappa_c/2\pi = 380$ kHz
Weak port coupling	$\kappa_{c,w}$	$\kappa_{c,w}/2\pi < 5$ kHz
Cavity internal loss	$\kappa_{c,int}$	$\kappa_{c,int}/2\pi < 10$ kHz
Qubit lifetime	T_1	$T_1 = 17$ μs
Ramsey time	T_2	$T_2 = 20$ μs
Optical cavity frequency	ω_o	$\omega_o/2\pi = 277$ THz
Optical cavity external coupling	$\kappa_{o,ext}$	$\kappa_{o,ext}/2\pi = 2.12$ MHz
Optical cavity linewidth	κ_o	$\kappa_o/2\pi = 2.68$ MHz
LC circuit frequency	ω_e	$\omega_e/2\pi = 7.938$ GHz
LC circuit external coupling	$\kappa_{e,ext}$	$\kappa_{e,ext}/2\pi = 1.42$ MHz
LC circuit linewidth (low pump power)	κ_e	$\kappa_e/2\pi \approx 1.6$ MHz
LC circuit linewidth (high pump power)	κ_e	$\kappa_e/2\pi \approx 2.7$ MHz
Mechanical mode frequency	ω_m	$\omega_m/2\pi = 1.45$ MHz
Intrinsic mechanical dissipation rate	γ_m	$\gamma_m/2\pi = 0.11$ Hz
Vacuum optomechanical coupling	g_o	$g_o/2\pi = 60$ Hz
Vacuum electromechanical coupling	g_e	$g_e/2\pi = 1.6$ Hz
Optical cavity mode matching	ε	$\varepsilon = 0.80$

Extended Data Table 2 | Contributions to the quantum efficiency

Parameter	Symbol	Value
Finite bandwidth	η_{bw}	See Eq. (9)
Microwave transmission loss	η_{mic}	$\eta_{mic} = 0.34$
cQED system cavity loss	η_{cav}	$\eta_{cav} > 0.96$
Optical detection efficiency	η_{opt}	$\eta_{opt} = 0.28$
Added noise	η_{noise}	$\eta_{noise} = (1 + N_t)^{-1} = N_{det}^{-1}$
Transducer efficiency	η_t	See Eq. (10)
Transducer gain	η_G	See Eq. (11)

Numerical values are not reported for contributions that depend on Γ_e or Γ_o.